ADVANCED MATERIALS
www.advmat.de

Concurrent Amorphization and Nanocatalyst Formation in Cu-Substituted Perovskite Oxide Surface: Effects on Oxygen Reduction Reaction at Elevated Temperatures

SungHyun Jeon, Wan-Gil Jung, Hohan Bae, Sejong Ahn, Bonjae Koo, WonJeong Yu, Seunghyun Kim, DongHwan Oh, Uisik Kim, Scott A. Barnett, Jongsu Seo,* Bong-Joong Kim,* and WooChul Jung**

The activity and durability of chemical/electrochemical catalysts are significantly influenced by their surface environments, highlighting the importance of thoroughly examining the catalyst surface. Here, Cu-substituted $La_{0.6}Sr_{0.4}Co_{0.2}Fe_{0.8}O_{3-\delta}$ is selected, a state-of-the-art material for oxygen reduction reaction (ORR), to explore the real-time evolution of surface morphology and chemistry under a reducing atmosphere at elevated temperatures. Remarkably, in a pioneering observation, it is discovered that the perovskite surface starts to amorphize at an unusually low temperature of approximately 100 °C and multicomponent metal nanocatalysts additionally form on the amorphous surface as the temperature raises to 400 °C. Moreover, this investigation into the stability of the resulting amorphous layer under oxidizing conditions reveals that the amorphous structure can withstand a high-temperature oxidizing atmosphere (≥650 °C) only when it has undergone sufficient reduction for an extended period. Therefore, the coexistence of the active nanocatalysts and defective amorphous surface leads to a nearly 100% enhancement in the electrode resistance for the ORR over 200 h without significant degradation. These observations provide a new catalytic design strategy for using redox-dynamic perovskite oxide host materials.

1. Introduction

The importance of green and sustainable energy technologies, such as fuel cells, continues to grow in response to global climate change.[1] Accordingly, there has been a significant focus on exploring fascinating electrocatalytic materials for developing efficient energy devices.[2] Among these materials, perovskite oxides (chemical formula: ABO_3) exhibit remarkable structural and chemical flexibility, enabling them to accommodate various elements. Hence, certain perovskite oxides exhibit high electronic and ionic conductivities, along with excellent catalytic activity, making them promising candidates for oxygen-involved electrochemical reactions such as the oxygen reduction reaction (ORR) and oxygen evolution reaction (OER).[3,4] However, despite significant advancements in perovskite oxide materials as electrocatalysts for energy devices,

---

S. Jeon, S. Ahn, W. Yu, S. Kim, D. Oh, U. Kim
Department of Materials Science and Engineering
Korea Advanced Institute of Science and Technology (KAIST)
Daejeon 34141, Republic of Korea

S. Jeon, H. Bae, S. A. Barnett
Department of Materials Science and Engineering
Northwestern University
Evanston, IL 60208, USA
E-mail: s-barnett@northwestern.edu

The ORCID identification number(s) for the author(s) of this article can be found under https://doi.org/10.1002/adma.202404103

[+] Present address: Korea Basic Science Institute, Gwangju Center, Gwangju 61186, Republic of Korea

DOI: 10.1002/adma.202404103

W.-G. Jung[+], B.-J. Kim
School of Materials Science and Engineering
Gwangju Institute of Science and Technology (GIST)
Gwangju 61005, Republic of Korea
E-mail: kimbj@gist.ac.kr

B. Koo
School of Chemistry and Energy
Sungshin Women's University
2 Bomun-ro 34da-gil, Seoul 02844, Republic of Korea

J. Seo
Hydrogen Research Department
Korea Institute of Energy Research (KIER)
152 Gajeong-ro, Yuseong-gu, Daejeon 34129, Republic of Korea
E-mail: jsseo@kier.re.kr

W. Jung
Department of Materials Science and Engineering
Seoul National University (SNU)
Seoul 08826, Republic of Korea
E-mail: wcjung@snu.ac.kr

challenges such as surface chemical instability and poor activity compared with precious metals remain critical obstacles to achieving widespread commercialization.[5]

The surface environment, such as the crystal structure or chemical composition, is recognized as a key factor that influences the durability and activity of catalysts.[5,6] Over the last decade, numerous surface-tailoring strategies and their effects on catalytic durability and activity have been extensively investigated to design exceptional electrocatalysts. For example, the introduction of highly active nanocatalysts (NCs) has received considerable attention as an efficient method for promoting surface chemical or electrochemical reactions using small amounts of catalyst.[7–9] In particular, the ex-solution technique, in which metal NCs spontaneously grow on the host oxide surface via a reduction heat treatment, has made remarkable achievements in various chemical and electrochemical fields. Compared with NCs dispersed using other methods, ex-solved NCs exhibit excellent thermal/chemical durability at high temperatures because they are embedded within the host oxide lattice in a socketed structure during their growth process.[10] This unique structure establishes a robust bond between the host oxide and NCs, imparting exceptional durability and unique catalytic properties. Therefore, a wide range of studies have been actively conducted involving the decoration of various compositions of NCs and in-depth investigations to comprehend the mechanism underlying the ex-solution phenomenon.[11–13]

However, the ex-solution process always requires high-temperature heat treatment under reducing conditions, making it challenging to apply this technique to representative catalyst materials such as Co/Fe-based perovskite oxides (La, Sr)(Co, Fe)O_3 (LSCF).[14–16] Although these materials are excellent catalysts, they exhibit poor phase stabilities under reducing conditions, such as in a hydrogen atmosphere, for example. To overcome this limitation, a compromise approach has been proposed: reducing the heat treatment under milder conditions for a very short period of time to produce extruded catalysts.[17–19] The key point is finding the right temperature window that allows for the extraction of the metal within a very short time without distorting the parent oxide phase. For example, Jung et al. reported the successful decoration of Ag NCs on $Ba_{0.95}Ag_{0.05}Co_{0.9}Ta_{0.1}O_{3-\delta}$ using ex-solution under 4% H_2/Ar atmosphere only at 300 °C for 2 h.[19] Similarly, previous literature has reported typical temperature windows and annealing times for ex-solution on air electrodes to be below 450 °C and approximately 3 h, respectively, to avoid the decomposition of parent oxides.[17–20] However, these previous studies have primarily focused on only extracting active NCs without causing bulk-phase decomposition; therefore, investigations on in-depth surface analysis, which determines reactivity and durability, remain relatively unexplored in comparison to studies conducted using redox-stable parent materials such as (La,Sr)MO_3 (M = Ti, Mn, Cr).

In parallel, controlling the surface crystallinity has been suggested as a potential method to improve the durability and activity of perovskite oxides. Skinner et al. reported that amorphous $La_{0.8}Sr_{0.2}CoO_{3-\delta}$ exhibits much higher oxygen diffusivity (D^*) and oxygen exchange kinetics (k^*) values than its crystalline counterpart.[21] They argued that its amorphous nature, with more defects and open sites than dense crystalline materials, facilitates the easier accommodation of Sr ions, suppressing their surface segregation, which is the primary reason for the performance degradation of solid oxide fuel cell (SOFC) electrodes. Furthermore, Shim et al. achieved the high-performance LSCF electrode by depositing partially amorphous $La_{0.6}Sr_{0.4}CoO_{3-\delta}$ (LSC) using atomic layer deposition.[22] In this report, density functional theory revealed that amorphous LSC has a significantly increased reactivity for the ORR owing to the low energy required for oxygen removal. However, because all previous studies have employed a bottom-up methodology using thin-film techniques, their applicability to diverse materials and practical applications is limited.

To address these challenges, in this study, we propose a new material design strategy that can simultaneously induce nanoparticle formation and surface amorphization through meticulous surface analysis of Co/Fe-based materials subjected to varying heat treatment conditions and durations. Using in situ and ex situ transmission electron microscopy (TEM) analysis, we explored the evolution of surface morphology of LSCF, a state-of-the-art SOFC cathode,[23–25] with Cu dopant, which is an earth-abundant metal and a good candidate for ORR catalysts.[26–28] Notably, we observed the disruption of the surface crystallinity of LSCF during the high-temperature reducing heat treatment in real time, followed by the formation of NC particles. We also found that the thicknesses of the amorphous layers increased as the heat-treatment time increased, thereby enhancing the stability of the resulting amorphous layer. In addition, the effects of the ex-solution and amorphization on the catalytic reaction were evaluated by analyzing the electrochemical properties via in situ reduction in the reactor. This reveals that the concurrent formation of the amorphous layer and NCs successfully enhanced the ORR activity by nearly 100% and significantly improved the durability of the host LSCF. To the best of our knowledge, this is the novel report of a real-time investigation of the surface evolution of Co/Fe-based perovskite oxides under a reducing atmosphere. Based on our observations, this study expands the concept of ex-solutions in terms of phase stability and provides new insights into material design using redox dynamic host materials.

2. Results and Discussion

2.1. Real-Time Observation of Cu-Doped LSCF: Surface Evolution Dynamics According to the Reduction Temperature

A series of $La_{0.6}Sr_{0.4}(Co_{0.2}Fe_{0.8})_{1-x}Cu_xO_3$ ($x = 0, 0.03, 0.1$) samples were prepared using the same conventional sol-gel method, with Cu substituting the B-site cations. These parent oxide materials were used to obtain nanoarchitectured ORR catalysts by reducing heat treatment. High-resolution X-ray diffraction (HR-XRD) analysis was performed on the synthesized powder mixed with Si powder as an internal standard, and the results are shown in **Figure 1**. We observed that the incorporation of 3 mol% Cu induced a positive peak shift compared with that of undoped LSCF, and no secondary phase was detected. However, 10 mol% Cu-doped LSCF showed a secondary phase peak, while the other peaks remained nearly in the same locations as those of 3 mol% Cu-doped LSCF, confirming that 3 mol% was within the solubility limit. The inductively coupled plasma optical emission spectroscopy (ICP-OES) results in Table S1 (Supporting Information)

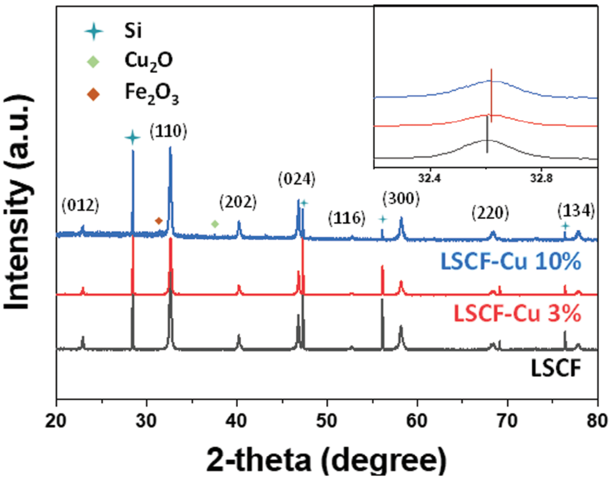

Figure 1. Physical characterization of Cu-doped LSCF system: HR-XRD results in different Cu amounts.

further demonstrate that 3 mol% Cu has successfully substituted the B-site in LSCF.

We conducted real-time observations of the surface morphology evolution of 3 mol% Cu-doped LSCF (hereafter referred to as LSCF-Cu) depending on the temperature using in situ high-resolution transmission electron microscopy (HR-TEM). To monitor the surface evolution under reducing atmosphere, LSCF-Cu particles were exposed to a 4% H_2/Ar gas environment at varying temperatures ranging from room temperature to 500 °C. Each temperature was maintained for 20 minutes. Representative TEM bright-field (BF) images, obtained at increased temperatures during the in situ reduction process, are presented in **Figure** 2a–f. Initially, an amorphous layer formed at 100 °C (Figure 2b), followed by a gradual increase in thickness (Figure 2c,d). Subsequently, the ex-solution of NCs became apparent at 400 °C (Figure 2e) as they penetrated the amorphous layer, and the NCs slightly grew further at 500 °C (Figure 2f). To confirm the presence of an amorphous layer on the surface, the fast Fourier transform (FFT) patterns of the interior region (red box in Figure S1b, Supporting Information) and the surface regions (blue box in Figure S1c, Supporting Information) were compared. The former exhibits a clear diffracted spot pattern of single crystalline while the latter shows a diffused ring associated with the amorphous surface layer, alongside the crystalline pattern.[6,29] The schematics in Figure 2j summarize the change in surface structure and morphology. Furthermore, energy-dispersive X-ray spectroscopy (EDS) analyses were performed with the same LSCF-Cu particle (Figure 2g). The scanning spectra in Line 1 (yellow arrow, Figure 2h) confirm that the ex-solved NCs mainly consist of Cu, while those along Line 2 (green arrow, Figure 2i) indicate that the surface amorphous layer is not a secondary phase or by-product but rather an amorphous LSCF layer with a cationic ratio similar to that of the bulk crystal.

It is noteworthy that the surface amorphization of LSCF-Cu occurs at a remarkably low temperature of approximately 100 °C. This phenomenon was attributed to the rapid release of lattice oxygen atoms near the LSCF surface, rather than the migration of heavier cations, as shown in previous studies.[30] This observation aligns with prior literatures, suggesting that oxygen liberation from oxides can occur at temperatures as low as 200 °C, even under a relatively moderate reducing atmosphere.[31,32] This trend was also consistent with the H_2-temperature programmed reduction (TPR) analysis (Figures S2, S3, Supporting Information) and thermogravimetric analysis (TGA)-differential scanning calorimetry (DSC) analysis (Figure S4, Supporting Information), despite the environmental differences compared to the in situ TEM analysis. Reports showing that LSCFs are unstable in reducing environments also support the facile release of these lattice oxygen ions, indicating that they exhibit dynamic oxygen nonstoichiometric behaviors.[33] Detailed examinations are discussed below, combining TPR and EDS mapping and the in situ X-ray photoelectron spectroscopy (XPS) results of LSCF and LSCF-Cu.

2.2. Investigation of Surface Nanoarchitecture Evolution and Oxygen Atmosphere Stability with Reduction Time

Considering the results discussed earlier, we verified that the exsolution of metal NCs and the amorphization of the oxide surface occurs simultaneously during reduction in a 4% H_2 environment in LSCF-Cu. However, since the LSCF cathode operates under high-temperature oxidizing conditions, i.e., ORR in SOFCs, it is crucial for the amorphous layer and ex-solved NCs, formed in a reducing atmosphere, to withstand the opposing oxidizing environment and effectively fulfill their purpose.

To explore the survivability of the amorphous layer, we hypothesized that the duration of the reduction process played a critical role. Initially, we focused on the impact of the reduction time, while keeping the reduction temperature constant. The ex situ HR-XRD analysis (Figure S5, Supporting Information) and phase decomposition expectation results (Figure S6, Supporting Information) show no significant secondary phases formed up to 500 °C under 4% H_2/Ar, but, a small secondary phase peak emerged at 600 °C, indicating the bulk phase separation of the LSCF.[34,35] Thus, 450 °C was selected as the reduction temperature and surface morphology evolution was observed by varying the retention time.

We then investigated the effect of duration on the initial surface morphology and survivability of the amorphous layer (**Figure** 3a). Specifically, we compared samples subjected to 2 h, which is a commonly employed short duration for Co/Fe-based perovskite ex-solutions,[17,19] and 10 h; a significantly increased duration was devised in this study at a fixed temperature of 450 °C under 4% H_2/Ar. Figure 3b,c displays the TEM BF images of an ex-solved NC with a LSCF-Cu support, taken after reduction at 450 °C for the durations of 2 and 10 h, respectively. It is observed that the amorphous layer thickens from 1.5 to 2.7 nm, as the duration increases. Subsequently, these samples were exposed to a synthetic air atmosphere at 650 °C for 30 h (Figure 3d,e). The ex-solved NCs remained without redissolving into their matrix, representing stability. However, the amorphous layer of the samples subjected to 2 h reduction completely disappeared (Figure 3d) whereas that of the sample subjected to 10 h reduction remained the same thickness (Figure 3e). These results highlight that an appropriate duration of reduction is essential for ensuring the stability of the surface amorphous layer. Figure S7 (Supporting Information) further confirms that the size and distribution

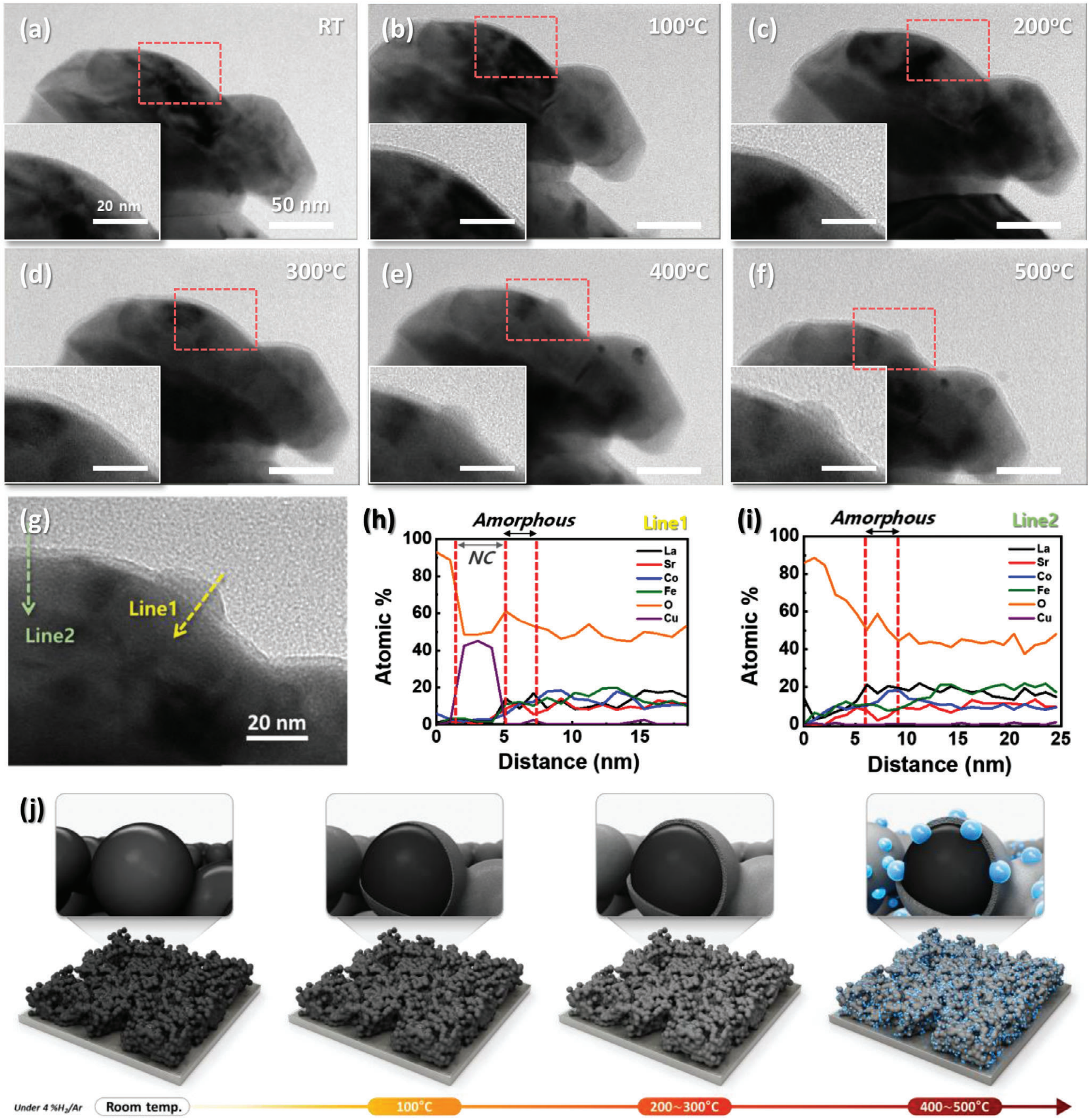

Figure 2. In situ TEM observation of both amorphization and ex-solution during the reduction process: TEM images at a) room temperature, b) 100 °C, c) 200 °C, d) 300 °C, e) 400 °C, and f) 500 °C. g) Magnified TEM images and h,i) corresponding EDS line scan results of LSCF-Cu particle. Finally j) a schematic illustration summarizes this observation.

of the NCs remained nearly unchanged after re-oxidation treatment, indicating the excellent thermal stability of the ex-solved NCs.[17–19,36,37] These findings highlight the importance of achieving the formation of nanoparticles and amorphous layers and ensuring their stability by employing an appropriate reduction process duration. This discovery is supported by previous literature, illuminating the diverse stability levels associated with varying degrees of amorphization in thin-film LSC.[38]

2.3. Impacts of Cu-Doping on Ex-Solution and Amorphization Behaviors

The effect of Cu-doping on the behavior of the ex-solution and amorphization must be discussed before evaluating the electrochemical properties. We observe that the distribution density of NCs in LSCF-Cu is much higher than that in pristine LSCF after the reducing heat treatment (**Figure** 4a,d). Furthermore,

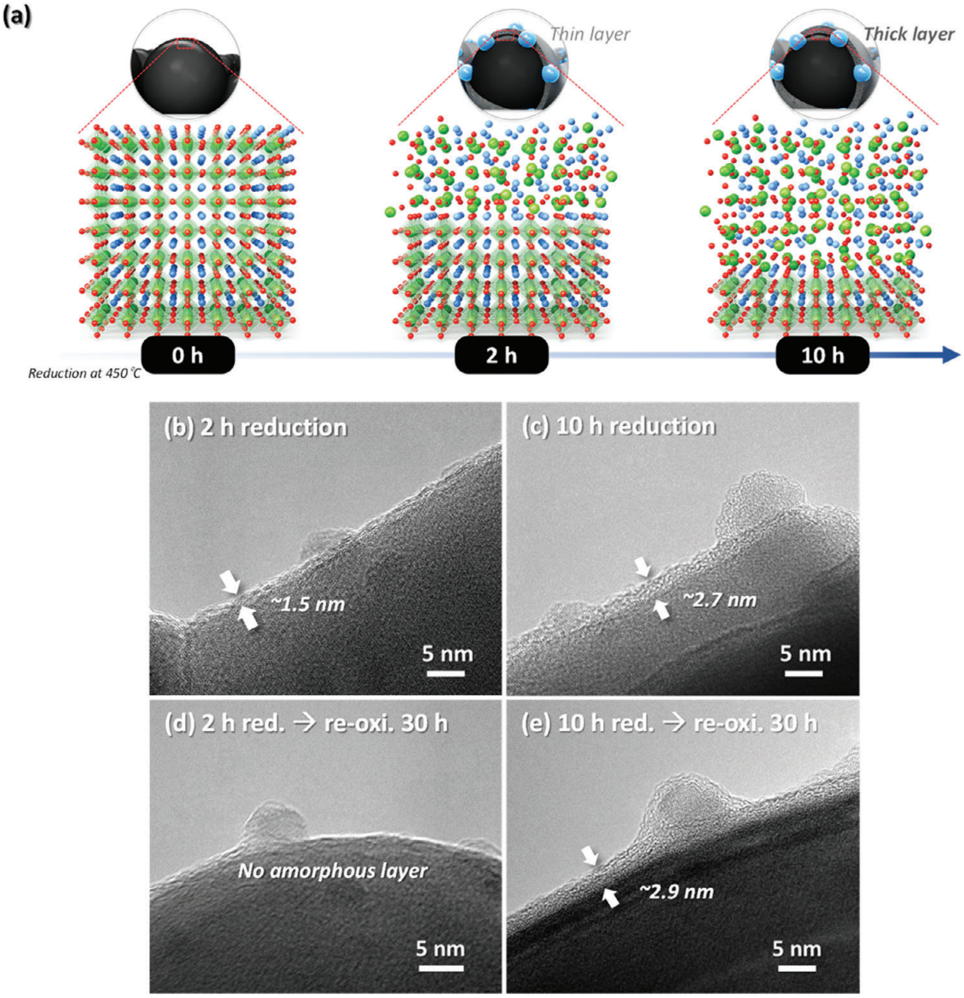

Figure 3. a) Schematic illustration of change of crystallinity according to the reduction time. TEM image of thickness and stability of amorphous layer in LSCF-Cu according to the reduction time. b) as-reduced for 2 h, c) 10 h, d) after reoxidation of 2 h reduction sample, and e) after reoxidation of 10 h reduction sample. The reduction and re-oxidation was conducted in a condition of [4% H_2, 450 °C] and [Air, 650 °C, 30 h], respectively.

HAADF-STEM images and their corresponding EDS mapping results of the two samples, shown in Figure 4b,e, indicate the difference in the composition of ex-solved NCs in LSCF-Cu and LSCF. Specifically, the NCs in LSCF-Cu predominantly consist of a copper-dominated Cu–Co–Fe alloy, whereas those in LSCF comprise a cobalt–iron (Co–Fe) alloy. The TEM BF images depicted in Figure 4c,f reveal that the formation of the amorphous layer occurred with a similar thickness, irrespective of the presence of Cu doping. This suggests that the strategy for amorphization remains effective regardless of Cu doping, as implied by forthcoming results.

Taken together, we performed a fitting of the H_2-TPR profile, identifying peaks and assigning their origins (Figure S2 and Table S2, Supporting Information). This analysis reveals that Cu-doping decreases the main reduction temperature for the ex-solution by approximately 50 °C (from 358.7 to 298.9 °C), which indicates a decrease in the bonding energy between transition metals and oxygen atoms. Thus, the incorporation of Cu significantly boosts the ex-solution, simultaneously leading to a modification in the composition of NCs. This observation is in line with previous literature, where changes in the bonding energy, chemical states, and bond lengths of elements occur upon doping with heterogeneous elements, leading to modifications in the ex-solution behavior.[39–41]

In situ XPS analysis results, as depicted in Figure S8 (Supporting Information), support these findings by revealing the surface chemical environment. Both the LSCF-Cu and LSCF samples were subjected to heating up to 500 °C within an XPS chamber under ultra-high vacuum conditions for analysis. The O 1s peak indicates a higher presence of defective O species, known to correlate strongly with surface oxygen vacancies, in LSCF-Cu compared to LSCF.[42–44] This also implies the inclusion of Cu in LSCF prompted the formation of additional oxygen vacancies in a reducing environment, suggesting a potential acceleration in the ex-solution process of nanoparticles.

To summarize the results obtained so far, as the temperature increased in a reducing atmosphere, an amorphous layer formed (100-200 °C) and nanoparticle ex-solution progressed (≈400 °C). Subsequently, at 450 °C, the thickness of the amorphous layer increased over time, enhancing the stability in an oxidizing

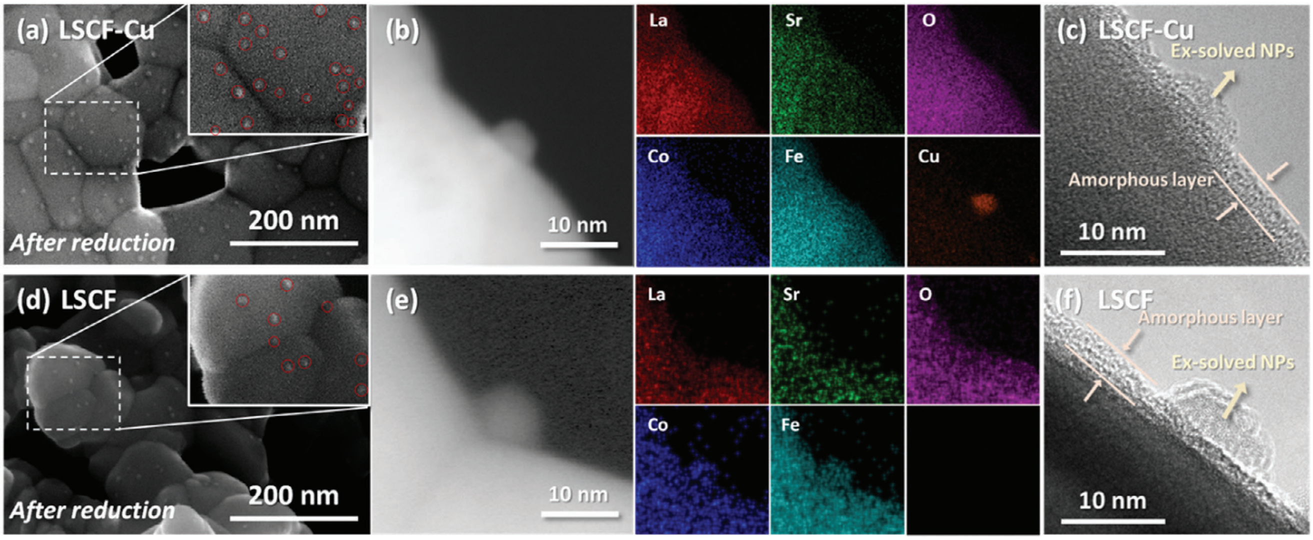

Figure 4. Comparison of ex-solution behavior according to Cu doping: a) SEM, b) HAADF-STEM & EDS, and c) TEM results of LSCF-Cu. d) SEM, e) HAADF-STEM & EDS, and f) TEM results of undoped LSCF.

atmosphere. Additionally, Cu doping altered the composition and distribution of the ex-solved nanoparticles.

2.4. Electrochemical Performance of LSCF-Based Cathode: Correlation with Ex-Solution and Surface Amorphization

To investigate the impact of the ex-solution and amorphization on the oxygen reduction reaction, electrochemical impedance spectroscopy (EIS) was conducted on the LSCF-Cu and LSCF cathodes under open-circuit voltage (OCV) conditions with symmetric cell configurations. To directly compare the results before and after reduction on a single sample, we devised a temperature and gas flow program for in situ reduction during the EIS measurements (Figure S9, Supporting Information). This design aims to eliminate ambiguity owing to errors in sample fabrication and clarify the observed effects. The measurements were performed on unreduced samples in air at temperatures ranging from 650 to 500 °C. Subsequently, the temperature was decreased to 450 °C, and the gas was changed to a mixture of 4% H_2 and 96% Ar for reduction. To prevent the reaction between O_2 and H_2, Ar gas was purged immediately before and after the reduction process. Additionally, measurements were performed on the reduced samples at temperatures ranging from 650 to 500 °C in air. Consequently, a direct comparison of the electrochemical performances at each temperature with and without the reduction process is possible.

Figure 5a–c displays a typical Nyquist plot at 500 °C, where the diameter of the impedance arc indicates the electrode resistance. To investigate the effects of ex-solution and amorphization on electrochemical performance, we prepared three LSCF-Cu samples and applied different reduction conditions to each sample, enabling a direct comparison before and after the reduction process. In Figure 5a, the impedance arc shows before and after reduction at 200 °C for 2 h, a temperature associated solely with surface amorphization according to in situ TEM and H_2-TPR findings. The absence of a noticeable disparity in the initial electrode resistance before and after the reduction suggests that the formation of an amorphous layer does not significantly affect the electrode resistance. Figure 5b,c shows the results before and after reduction, at 450 °C for 2 and 10 h, respectively; reduction conditions at which ex-solution and surface amorphization occur. Despite the differences in the stability of the amorphous layer under high-temperature oxidizing conditions, both samples exhibited similar decreases in electrode resistance after the reduction process. In summary, these findings indicate that the ex-solution of NCs, and not the amorphous layer, plays a significant role in improving the initial electrode performance. The Arrhenius plot presented in Figure 5d, distribution of relaxation time (DRT) analysis presented in Figure S10 (Supporting Information), and fitted impedance arc (Figure S11 and Table S3, Supporting Information) reveal that the ex-solved Cu–Co–Fe NCs predominantly enhance the surface oxygen exchange reaction, which is the main obstacle of LSCF, thereby slightly decreasing the activation barrier from 1.47 to 1.31 eV.[45,46] It is believed that the enhanced performance is due to the composition of nanocatalyst, which improves the surface oxygen adsorption/incorporation step through the redox flexibility of CuO_x.

A 100 h operation test was conducted to assess the impact of the amorphous layer, as depicted in Figure 5e,f. Figure 5f presents the results of converting the y-axis in Figure 5e into the degree of degradation ($R_p/R_{p,\text{ initial}}$). Four samples were prepared for the stability comparison: unreduced LSCF-Cu, LSCF-Cu reduced at 200 °C for 2 h, LSCF-Cu reduced at 450 °C for 2 h, and LSCF-Cu reduced at 450 °C for 10 h. The electrode resistance increased by approximately 27% over 90 h for unreduced LSCF-Cu, which is consistent with the deterioration attributed to the Sr segregation of LSCF in the OCV reported in the literature.[25,47–49] The XPS analysis of Sr 3d spectra of LSCF-Cu after annealing in air at 650 °C presented in Figure S12a (Supporting Information) shows the formation of large amount of $\text{Sr}_{\text{surface}}$ peak. Similarly, LSCF-Cu reduced at 200 °C for 2 h and LSCF-Cu reduced at 450 °C for 2 h exhibited comparable degradation rates. Although

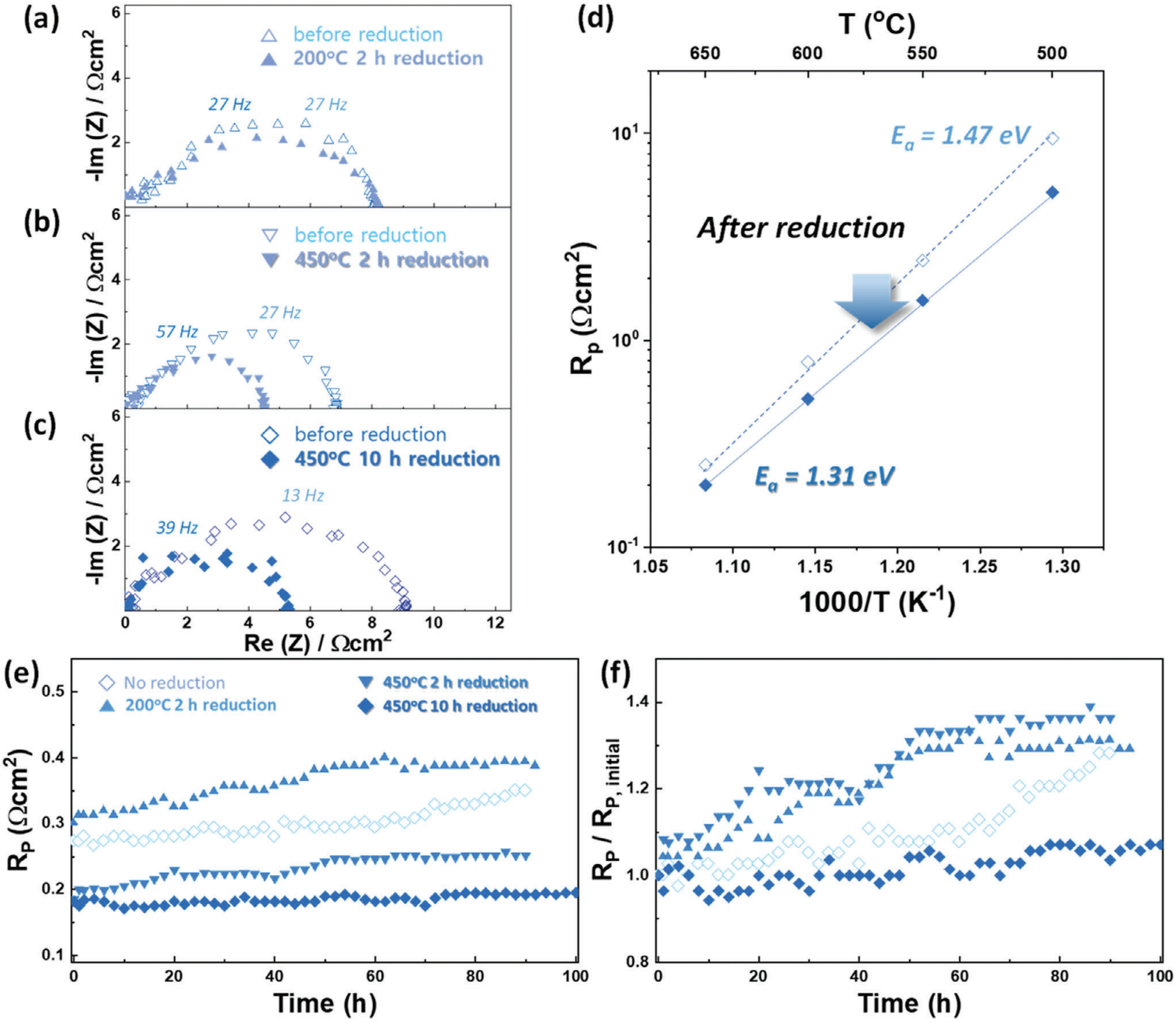

Figure 5. Electrochemical impedance spectra of LSCF-Cu according to reduction condition: Initial Nyquist plot measured at 500 °C before and after reduction at a) 200 °C for 2 h, b) 450 °C for 2 h, and c) 450 °C for 10 h. d) Arrhenius plot for LSCF-Cu with and without reduction. e) The long-term stability test at 650 °C. Graph f) presents the degree of degradation by changing the y-axis of e) as $R_P/R_{P,\ initial}$.

they initially had an amorphous layer, they vanished upon recrystallization in an oxidizing atmosphere, rendering them incapable of inhibiting Sr segregation. Conversely, LSCF-Cu reduced at 450 °C for 10 h demonstrated stable electrode performance for the entire 100 h of duration, unlike the aforementioned three samples. This is supported by the HR-TEM analysis results after the stability test, shown in Figures S13, S14 (Supporting Information), which verifies the survivability of amorphous layer, unlike the previously mentioned three samples. The XPS Sr 3d spectra of 450 °C 10 h reduced LSCF-Cu after annealing in the air also support this stability result, showing much less $Sr_{surface}$ peak (Figure S12b, Supporting Information). This can be attributed to the amorphous layer having numerous open sites, allowing it to effectively accommodate the Sr ions that migrate near the surface.[50,51] Consequently, the formation of a Sr-rich second phase on the electrode surface and an Sr-deficient layer near the surface may not occur, thus suppressing the associated deterioration.[38,47]

To confirm the application versatility of this strategy, we investigated the difference in electrochemical properties of both undoped and Cu-doped LSCF by applying the best reduction condition of 450 °C for 10 h. **Figure 6** illustrates the changes in electrode resistance for the initial and long-term operations before and after the reduction of LSCF and LSCF-Cu. Figure 6a shows that there was almost no decrease in the initial electrode resistance in LSCF, in contrast to that in LSCF-Cu. This disparity is attributed to the different distribution densities and compositions of the NCs according to Cu-doping. However, the long-term stability test shown in Figure 6b shows that the formation of an amorphous layer on the electrode surface can

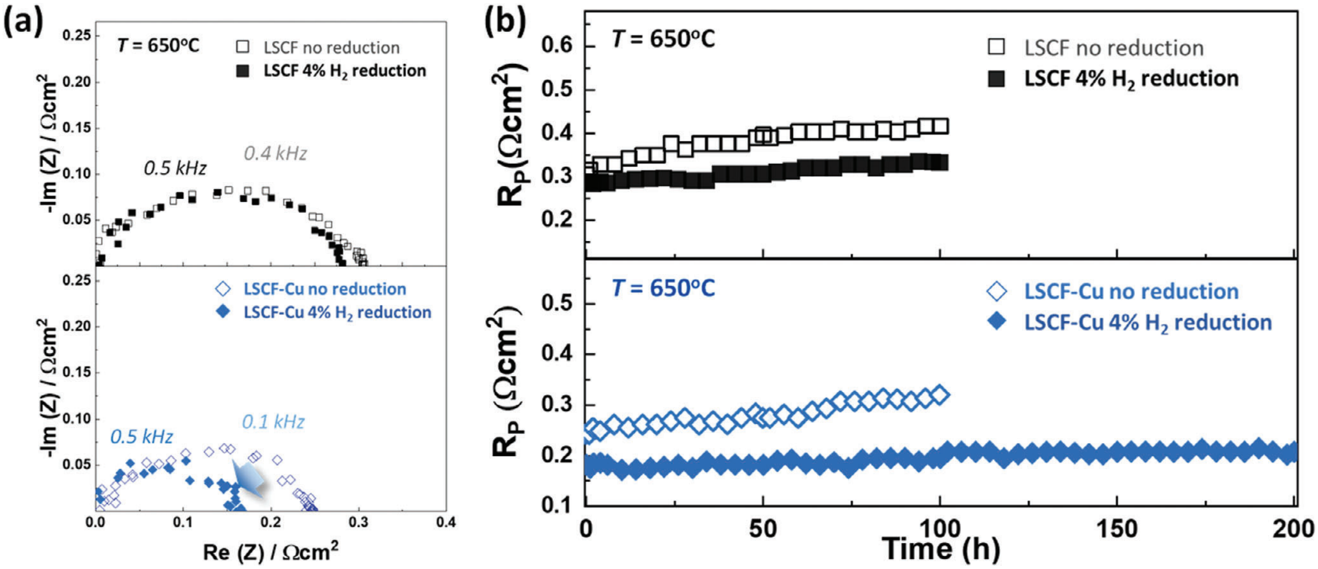

Figure 6. Evaluation the effect of ex-solution and the amorphization of LSCF-based cathode according to Cu-doping: a) Nyquist plot at 650 °C. b) The long-term stability test at 650 °C of LSCF and LSCF-Cu before and after reduction.

prevent the degradation of LSCF-based electrodes to a similar level irrespective of Cu-doping. These findings reaffirm the contribution of Cu ex-solution to initial ORR activity, while demonstrating that the amorphization of the LSCF surface enhances stability. Using this approach, we were able to demonstrate an LSCF-Cu electrode with a sustained low electrode resistance of approximately 0.18 Ω cm^2 over 200 h and significantly alleviated degradation.

Figure 7 shows a demonstration of the impact and the feasibility of the concurrent ex- solution and amorphization in single-cell test. The detailed configuration of single cell is shown in cross-SEM image in Figure S15 (Supporting Information) and

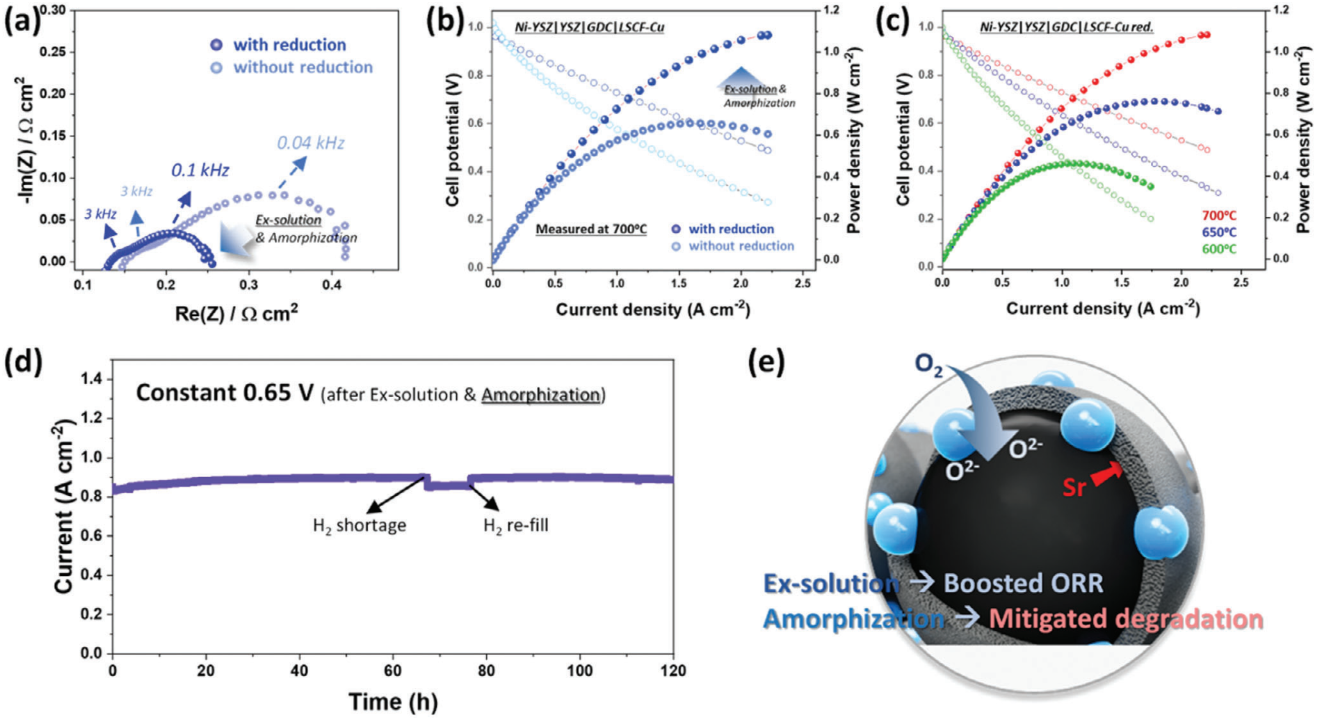

Figure 7. Application of in situ ex-solution and amorphization strategies to single-cell measurement: a) Nyquist plot with/without reduction of Ni-YSZ|YSZ|GDC|LSCF-Cu single-cell. *I–V–P* curve b) in comparison of with/without reduction and c) in different temperature. d) Stability test under constant 0.65 V at 650 °C, e) a schematic diagram summarizing the effect of ex-solution and amorphization.

the temperature and gas-flow during in situ reduction and cell activation were conducted through the protocol depicted in Figure S16 (Supporting Information). Figure 7a presents the EIS spectra of Ni-YSZ|YSZ|GDC|LSCF-Cu single cell at 700 °C with and without 4% H_2-450 °C-10 h of reduction. The ex-solution reduces the polarization resistance from 0.27 to 0.12 Ω cm^2, which is attributed through the decrease of impedance arc in cathode side located in relatively low frequency region. The peak power density (PPD) in *I*–*V* curve is corresponding with the EIS results (Figure 7b). The ex-solution improved the actual ORR of LSCF-Cu, promoting the PPD at 700 °C from 0.66 to 1.08 W cm^{-2}, which is an almost 64% enhancement. The PPD of ex-solved fuel cell at different operating temperature was depicted in Figure 7c, showing around 1.08, 0.76, 0.46 W cm^{-2} of peak power density (PPD) at 700–600 °C, respectively. The stability test at 650 °C under constant potential of 0.65 V presented in Figure 7d demonstrates the effect of amorphization on fuel cell. The stable amorphous layer induced through 4% H_2-450 °C-10 h of reduction realizes the stable performance over 120 h without any significant degradation, even using ambient air at cathode side.

2.5. Further Discussion

Lastly, we extended this strategy to various materials to provide broader applicability guidelines. First, we explored expanding the range of electrode materials for the amorphization strategy. We predicted that the reducibility of B-site cations would facilitate the formation of an amorphous layer. To test this, we performed HR-TEM analysis on three electrode materials with different B-site cations: $PrBaCo_2O_{5+\delta}$ (PBC) with Co, $La_{0.75}Sr_{0.25}Cr_{0.5}Mn_{0.5}O_{3\text{-}\delta}$ (LSCrM) with Cr/Mn, and $SrTiO_{3\text{-}\delta}$ (STO) with Ti, after they were reduced in 4% H_2 at 450 °C for 10 h, as shown in Figure S17 (Supporting Information). The analysis revealed that PBC, containing Co at the B-site, developed a distinct amorphous layer similar to LSCF after reduction. In contrast, the LSCrM and STO electrodes, which feature less reducible B-site cations (Cr/Mn and Ti, respectively), did not form any visible amorphous layers even after undergoing the same reduction process. This underscores the crucial role of B-site cation reducibility in the amorphization strategy; without reducible B-site cations, forming an amorphous layer is challenging.

Second, we explored expanding dopant selection for the ex-solution strategy by testing Ru, a known ORR/OER catalyst suitable for doping at the B-site. We fabricated an electrode by substituting 3% Ru at the B-site of LSCF. Following the same reduction treatment, the LSCF-Ru electrode showed improvements in both initial performance and stability (Figure S18, Supporting Information), attributed to the ORR catalytic properties of Ru nanoparticles and the formation of an amorphous layer.

In summary, if the B-site ion of perovskite oxide is highly reducible (e.g., Co or Fe) and the dopant has catalytic properties for the target reaction, the performance and durability improvement strategy through concurrent amorphization and ex-solution can be extended to various materials and applications. This may include other solid oxide and protonic ceramic electrochemical cell electrode materials such as $Ba_{1\text{-}x}Sr_xCo_{1\text{-}y}Fe_yO_{3\text{-}\delta}$ (BSCF), $Sm_xSr_{1\text{-}x}CoO_{3\text{-}\delta}$ (SSC), $BaCo_{1\text{-}y}Ta_yO_{3\text{-}\delta}$ (BCT), $PrNi_{1\text{-}y}Co_yO_{3\text{-}\delta}$ (PNC), and others.[54]

Nowadays, the amorphous nature has received great attention owing to its unique chemical/electrochemical properties resulting from its abundant defect concentration.[51–53] We induced this amorphization simultaneously with nanoparticle ex-solution by selecting suitable materials and using a straightforward reduction process. This approach is economically viable within an industrial context for several reasons. First, in contrast to prevailing amorphization studies confined to bottom-up fabrication solely in thin-film formats,[21,22,38] our methodology employs a top-down approach to generate an amorphous layer on the surface of a bulk porous electrode, which is deemed a more realistic and scalable approach. Second, within a practical SOFC systems, merely introducing a reduction treatment during the hydrogen preannealing step after all manufacturing stages, including stacking and sealing, can significantly enhance both performance and durability. Third, this strategy is versatile, extending beyond specific materials or applications, and can be adapted by carefully selecting various reducible B-site cations and catalytic dopants. We are confident that this strategy will not only activate a range of high-temperature catalytic reactions but also facilitate their practical implementation in industry.

3. Conclusion

In this study, a comprehensive observation of the surface morphology evolution of a Co/Fe-based perovskite oxide under a reducing atmosphere was performed by combining in situ and ex situ TEM analyses. We succeeded in fabricating a novel nanoarchitecture comprising of NCs and an amorphous surface layer. Our observations demonstrated that the surface undergoes preferential amorphization starting from a low temperature of 100°C, and subsequently the formation of a metal NCs occurs on the amorphous layer. Moreover, an investigation was performed on the behavior of NC formation and development of an amorphous layer at 450 °C depending on the duration. Remarkably, our findings revealed that subjecting the material to a reduction treatment at 450 °C for a duration of 10 h preserved the NCs and amorphous layer structures, even when exposed to a high-temperature oxidizing atmosphere. Finally, we evaluated the electrochemical properties of the fabricated electrode and remarkable improvements in activity and durability were observed. We believe that this study can open up a new strategy for expanding material candidates from redox-stable materials such as Mn-, Cr-, and Ti-based perovskite oxides to redox-dynamic materials such as Ni-, Co-, and Fe-based perovskite oxides for developing novel nanoarchitecture catalysts using ex-solution techniques.

4. Experimental Section

Sample Preparation: The LSCF and LSCF-Cu powder was synthesized through a conventional sol-gel method. First, metal (La, Sr, Co, Fe) nitrate precursors were dissolved in deionized water in a ratio of 6:4:2:8, followed by adding proper amounts of ethylene-diamine-tetraacetic acid (EDTA) and citric acid to the deionized water as a chelating agent in a ratio of metal:citric acid:EDTA = 2:3:1. Ammonium hydroxide (NH_4OH) was used to adjust the pH of the solution to 9, also creating a soluble environment for the EDTA. The mixed solution was stirred overnight at 170 °C for gelation and was then fired at 450 °C for 3 h in a heating mantle. Finally, calcination was carried out in a furnace at 900 °C for 8 h. An

LSCF-Cu powder was synthesized by substitutional doping of 3% and 10% of B-site cation with Cu using cooper nitrate precursor under the same conditions.

For half-cell, a single-crystal Y_2O_3-stabilized ZrO_2 substrate (YSZ, $Y_{0.08}Zr_{0.92}O_{1.96\text{-}\delta}$) was used as a solid electrolyte. Gd-doped CeO_2 ($Ce_{0.9}Gd_{0.1}O_{2\text{-d}}$, GDC) was deposited onto both sides of the YSZ to a thickness of 100 nm through a pulsed laser deposition (PLD) to prevent an undesired reaction between LSCF and YSZ electrolyte. The synthesized LSCF and LSCF-Cu powder were mixed with ink vehicle and ethanol by ball milling overnight to form a slurry. The LSCF and LSCF-Cu ink slurry were tape-casted onto both sides of a GDC-deposited YSZ electrolyte, followed by sintering at 950 °C for 1 h to form a porous structure.

The comprehensive process for single-cell fabrication is outlined in more detail elsewhere.[55] In brief summary, slurries were formed using a combination of NiO powder (Fuel cell materials) and YSZ-8 powder (Tosoh) in a ratio of 39 wt% NiO to 39 wt% YSZ, supplemented with 9% starch (except in the case of the functional layer) to introduce porosity in the support layer. For the electrolyte tapes, Fe_2O_3 (Alfa Aesar) was included as a sintering aid at a concentration of 1 wt%. The anode support layer (ASL), anode functional layer (AFL), and electrolyte layer were co-sintered at 1290 °C for 4 h. A GDC buffer layer was applied onto the electrolyte layer and sintered at 1100 °C for 1 h. Subsequently, an LSCF-Cu cathode with an area of 0.5 cm^2 was sintered at 950 °C for 1 h.

Physical Characterization: X-ray diffraction (XRD, Rigaku RU300, Tokyo, Japan, Cu K α wavelength ($\lambda = 1.541$Å)) analysis of the synthesized and reduced powder was conducted. The H_2-temperature programmed reduction (TPR) analysis was conducted by flowing 10%H_2-90%Ar gas and detecting the gas concentration changes with a quadrupole mass spectrometer (Autochem II, Micromeritics). The pre-heat treatment at 300 °C for 1 h flowing 5% O_2 gas was conducted in advance to TPR analysis. The morphology of ex-solved nanoparticles was examined by scanning electron microscopy (SEM, Hitachi S-4800). An ex situ transmission electron microscopy (TEM, Talos F200X) was employed at 200 kV to confirm the ex-solution and amorphization. By using the high-angle annular dark-field scanning TEM (HAADF-STEM) mode, the sample morphology and composition were analyzed. For real-time observation, an in situ gas flow holder (Hummingbird Scientific) and transmission electron microscopy (TEM, Tecnai G2, F30 S-Twin, operating at 300 keV, FEI) were utilized to observe the ex-solution of nanoparticles and the amorphization of LSCF crystals at different temperatures (RT-500 °C) under 4% H_2/Ar gas flow.

Electrochemical Measurement: The electrochemical properties of symmetrical cells, consisting of screen-printed cathodes on both sides of the electrolyte, were investigated with electrochemical impedance spectroscopy (EIS, VSP-300, Biologic) under a synthetic air atmosphere in a temperature range of 650–500 °C in an open-circuit voltage (OCV) condition. Before measurement, a reduction in diluted hydrogen (4% H_2 and 96%Ar) atmosphere was conducted for simultaneous ex-solution and amorphization. A perturbation voltage amplitude (V_a) of 40 mV and a frequency range of 1 MHz–10 mHz was selected. The synthetic air (21% of O_2 and 79% of Ar) was delivered in a controlled manner by digital mass flow controllers with a total flow rate of 100 sccm under standard temperature and pressure levels. The symmetrical cell measurements were conducted with the silver paste as a current collector using a mesh-type alumina reactor. DRT analyses were conducted with DRT tools and software obtained from Ciucci's group.[46] Single-cell measurement was conducted with a configuration of Ni-YSZ(ASL & AFL)|YSZ|GDC|LSCF-Cu. The temperature & gas flow change during in situ reduction and increasing temperature were conducted as depicted in Figure S16 (Supporting Information). For the measurement, a 100 standard cubic centimeters per minute (sccm) flow of humidified H_2 (97% H_2–3% H_2O) was supplied to anode side while 150 sccm air was supplied to the cathode side. Ambient air was utilized instead of laboratory air to replicate conditions more akin to the real environment. *I–V* curves were measured at 20 mV increments over the relevant voltage ranges for fuel cell operation. A constant potential of 0.65 V was consistently induced during the stability test.

Supporting Information

Supporting Information is available from the Wiley Online Library or from the author.

Acknowledgements

This work was supported by the National Research Foundation of Korea (NRF) grant funded by the Korean government (MSIT) (RS-2024-00436418, NRF-2023R1A2C3005190, 2021R1A2C1005741), Korea Institute of Energy Technology Evaluation and Planning (KETEP) and the Ministry of Trade, and the Ministry of Trade, Industry & Energy (MOTIE) of the Republic of Korea (No. 20218520040040), and Ceramic Strategic Technology R&D program through the Korea Institute of Ceramic Engineering & Technology (KICET) (grant NTIS no. 1415187241). SAB gratefully acknowledges financial support from the US Department of Energy Basic Energy Sciences under grant # DE-SC0016965. SHJ would like to express gratitude to all of the group members in the SAB group including Jakob Reinke for the assistance in this work.

Conflict of Interest

The authors declare no conflict of interest.

Author Contributions

S.H.J., W.-G.J., and H.B. contributed equally to this work. S.A.B., J.S., B.-J.K., and W.C.J. conceived and supervised the project. S.H.J., J.S., and W.C.J. contributed to conceptualization. S.H.J. performed the following experiments: electrochemical performance evaluation of symmetrical cell and DRT, SEM, ex situ TEM, and XPS analyses. J.S. performed the XRD, SEM, and TEM analysis. W.-G.J. conducted in situ TEM analysis. H.B. conducted a single-cell measurement. S.A. synthesized the materials and conducted XRD analysis. S.K. and B.K. conducted H_2-TPR analysis. D.H.O. contributed ex situ TEM. U.K. performed TGA-DSC analysis. W.J.Y. contributed to an XPS analysis. S.H.J., W.-G.J., and H.B. contributed to the writing of the manuscript. S.A.B., J.S., B.-J.,K., and W.C.J. contributed to the supervising the manuscript.

Data Availability Statement

The data that support the findings of this study are available from the corresponding author upon reasonable request.

Keywords

ex-solution, in situ observation, oxygen reduction reaction, solid oxide fuel cell, surface amorphization

Received: March 20, 2024
Revised: July 8, 2024

---

[1] Z. Shao, S. M. Haile, *Nature* **2004**, *431*, 170.
[2] S. Park, J. M. Vohs, R. J. Gorte, *Nature* **2000**, *404*, 265.
[3] J. Hwang, R. R. Rao, L. Giordano, Y. Katayama, Y. Yu, Y. Shao-Horn, *Science* **2017**, *358*, 751.
[4] D. Guan, H. Xu, Q. Zhang, Y. Huang, C. Shi, Y. Chang, X. Xu, J. Tang, Y. Gu, C. Pao, *Adv. Mater.* **2023**, *35*, 2305074.

[5] Y. Cao, M. J. Gadre, A. T. Ngo, S. B. Adler, D. D. Morgan, *Nat. Commun.* **2019**, *10*, 1346.
[6] T. G. Yun, Y. Sim, Y. Lim, D. Kim, J.-S. An, H. Lee, Y. Du, S.-Y. Chung, *Mater. Today* **2022**, *58*, 221.
[7] J. H. Kim, J. Hong, D.-K. Lim, S. Ahn, J. Kim, J. K. Kim, D. Oh, S. Jeon, S.-J. Song, W. Jung, *Energy Environ. Sci.* **2022**, *15*, 1097.
[8] J. Seo, S. Jeon, S. Lee, D.-K. Lim, J. H. Kim, J. H. Kim, S. Ahn, W. Jung, *ACS Catal.* **2022**, *12*, 8593.
[9] S. Nam, J. Kim, H. Kim, S. Ahn, S. Jeon, Y. Choi, B. Park, W. Jung, *Adv. Mater.* **2024**, *36*, 2307286.
[10] D. Neagu, G. Tsekouras, D. N. Miller, H. Ménard, J. T. S. Irvine, *Nat. Chem.* **2013**, *5*, 916.
[11] M. Zhu, P. Tian, R. Kurtz, T. Lunkenbein, J. Xu, R. Schlögl, I. E. Wachs, Y. Han, *Angew. Chem.* **2019**, *131*, 9181.
[12] J. K. Kim, S. Kim, S. Kim, H. J. Kim, K. Kim, W. Jung, J. W. Han, *Adv. Mater.* **2022**, *35*, 2203370.
[13] J. Myung, D. Neagu, D. N. Miller, J. T. S. Irvine, *Nature* **2016**, *537*, 528.
[14] S. Tao, J. T. S. Irvine, *Nat. Mater.* **2003**, *2*, 320.
[15] A. I. Tsiotsias, B. Ehrhardt, B. Rudolph, L. Nodari, S. Kim, W. Jung, N. D. Charisiou, M. A. Goula, S. Mascotto, *ACS Nano* **2022**, *16*, 8904.
[16] K. Kim, B. Koo, Y.-R. Jo, S. Lee, J. K. Kim, B.-J. Kim, W. Jung, J. W. Han, *Energy Environ. Sci.* **2020**, *13*, 3404.
[17] Y. Zhu, W. Zhou, R. Ran, Y. Chen, Z. Shao, M. Liu, *Nano Lett.* **2016**, *16*, 512.
[18] R. Sažinas, K. B. Andersen, S. B. Simonsen, P. Holtappels, K. K. Hansen, *J. Electrochem. Soc.* **2019**, *166*, F79.
[19] J. H. Kim, J. K. Kim, H. G. Seo, D. K. Lim, S. J. Jeong, J. Seo, J. Kim, W. C. Jung, *Adv. Funct. Mater.* **2020**, *30*, 2001326.
[20] R. Sažinas, K. B. Andersen, K. K. Hansen, *J. Solid State Electrochem.* **2020**, *24*, 609.
[21] A. Cavallaro, S. S. Pramana, E. Ruiz-Trejo, P. C. Sherrell, E. Ware, J. A. Kilner, S. J. Skinner, *Sustainable Energy Fuels* **2018**, *2*, 862.
[22] H. J. Choi, K. Bae, S. Grieshammer, G. D. Han, S. W. Park, J. W. Kim, D. Y. Jang, J. Koo, J. Son, M. Martin, J. H. Shim, *Adv. Energy Mater.* **2018**, *8*, 1802506.
[23] Y. Niu, Y. Zhou, W. Lv, Y. Chen, Y. Zhang, W. Zhang, Z. Luo, N. Kane, Y. Ding, L. Soule, *Adv. Funct. Mater.* **2021**, *31*, 2100034.
[24] H. Bae, Y. Shin, L. Mathur, D. Lee, S.-J. Song, *J. Korean Ceram. Soc.* **2022**, *59*, 876.
[25] S. Jeon, J. Seo, J. W. Shin, S. Lee, H. G. Seo, S. Lee, N. Tsvetkov, J. Kim, J. An, W. Jung, *Chem. Eng. J.* **2022**, *455*, 140611.
[26] C. Gao, Y. Liu, K. Xi, S. Jiao, R. I. Tomov, R. V. Kumar, *Electrochim. Acta* **2017**, *246*, 148.
[27] D. Mahato, T. Gurusamy, S. K. Jain, K. Ramanujam, P. Haridoss, T. Thomas, *Mater. Today Chem.* **2022**, *26*, 101167.
[28] J. Choi, J. T. Song, H. S. Jang, M.-J. Choi, D. M. Sim, S. Yim, H. Lim, Y. S. Jung, J. Oh, *Electron. Mater. Lett.* **2017**, *13*, 57.
[29] S. Yagi, I. Yamada, H. Tsukasaki, A. Seno, M. Murakami, H. Fujii, H. Chen, N. Umezawa, H. Abe, N. Nishiyama, *Nat. Commun.* **2015**, *6*, 8249.
[30] S. Arumugam, J. Shi, D. P. Tunstall, C. A. Vincent, *J. Phys.: Condens. Matter* **1993**, *5*, 153.
[31] J. R. Dahn, E. W. Fuller, M. Obrovac, U. Von Sacken, *Solid State Ionics* **1994**, *69*, 265.
[32] S. Sharifi-Asl, J. Lu, K. Amine, R. Shahbazian-Yassar, *Adv. Energy Mater.* **2019**, *9*, 1900551.
[33] K. J. Kim, C. Lim, K. T. Bae, J. J. Lee, M. Y. Oh, H. J. Kim, H. Kim, G. Kim, T. H. Shin, J. W. Han, *Appl. Catal., B* **2022**, *314*, 121517.
[34] H. Chang, H. Chen, Z. Shao, J. Shi, J. Bai, S.-D. Li, *J. Mater. Chem. A* **2016**, *4*, 13997.
[35] S. Hashimoto, Y. Fukuda, M. Kuhn, K. Sato, K. Yashiro, J. Mizusaki, *Solid State Ionics* **2010**, *181*, 1713.
[36] S. Liu, Q. Liu, J.-L. Luo, *J. Mater. Chem. A* **2016**, *4*, 17521.
[37] A. J. Carrillo, K. J. Kim, Z. D. Hood, A. H. Bork, J. L. M. Rupp, *ACS Appl. Energy Mater.* **2020**, *3*, 4569.
[38] J. Januschewsky, M. Ahrens, A. Opitz, F. Kubel, J. Fleig, *Adv. Funct. Mater.* **2009**, *19*, 3151.
[39] S. Joo, A. Seong, O. Kwon, K. Kim, J. H. Lee, R. J. Gorte, J. M. Vohs, J. W. Han, G. Kim, *Sci. Adv.* **2020**, *6*, eabb1573.
[40] S. Joo, O. Kwon, K. Kim, S. Kim, H. Kim, J. Shin, H. Y. Jeong, S. Sengodan, J. W. Han, G. Kim, *Nat. Commun.* **2019**, *10*, 697.
[41] T. Zhu, H. E. Troiani, L. V. Mogni, M. Han, S. A. Barnett, *Joule* **2018**, *2*, 478.
[42] H. Chen, C. Lim, M. Zhou, Z. He, X. Sun, X. Li, Y. Ye, T. Tan, H. Zhang, C. Yang, *Adv. Sci.* **2021**, *8*, 2102713.
[43] Y. Lee, D. Yoon, S. Yu, H. Sim, Y. Park, Y. Nam, K. Kim, S. Choi, Y. Kang, J. Son, *Adv. Mater.* **2022**, *34*, 2107650.
[44] B. Hua, M. Li, Y. Zhang, Y. Sun, J. Luo, *Adv. Energy Mater.* **2017**, *7*, 1700666.
[45] J. H. Kim, K. Jang, D.-K. Lim, S. Ahn, D. Oh, H. Kim, J. Seo, P.-P. Choi, W. Jung, *J. Mater. Chem. A* **2022**, *10*, 2496.
[46] M. Saccoccio, T. H. Wan, C. Chen, F. Ciucci, *Electrochim. Acta* **2014**, *147*, 470.
[47] B. Koo, K. Kim, J. K. Kim, H. Kwon, J. W. Han, W. C. Jung, *Joule* **2018**, *2*, 1476.
[48] R. I. Tomov, T. B. Mitchel-Williams, R. Maher, G. Kerherve, L. Cohen, D. J. Payne, R. V. Kumar, B. A. Glowacki, *J. Mater. Chem. A* **2018**, *6*, 5071.
[49] S. E. Jo, S. Jeon, H. J. Kim, B. C. Yang, K. Ju, T. M. Gür, W. Jung, J. An, *Small Methods* **2024**, *8*, 2300790.
[50] J. Liu, Y. Ji, J. Nai, X. Niu, Y. Luo, L. Guo, S. Yang, *Energy Environ. Sci.* **2018**, *11*, 1736.
[51] H. Shin, J. Seo, S. Jeon, S. J. Jeong, J. Kim, S. Lee, J. J. Lee, W. Jung, *J. Mater. Chem. A* **2024**, *12*, 10695.
[52] S. Liu, S. Geng, L. Li, Y. Zhang, G. Ren, B. Huang, Z. Hu, J.-F. Lee, Y.-H. Lai, Y.-H. Chu, *Nat. Commun.* **2022**, *13*, 1187.
[53] J. Bak, T. G. Yun, J.-S. An, H. Bin Bae, S.-Y. Chung, *Energy Environ. Sci.* **2022**, *15*, 610.
[54] J. H. Kim, D. Kim, S. Ahn, K. J. Kim, S. Jeon, D.-K. Lim, J. K. Kim, U. Kim, H.-N. Im, B. Koo, K. T. Lee, W. Jung, *Energy Environ. Sci.* **2023**, *16*, 3803.
[55] H. Wang, K. J. Yakal-Kremski, T. Yeh, G. M. Rupp, A. Limbeck, J. Fleig, S. A. Barnett, *J. Electrochem. Soc.* **2016**, *163*, F581.